

Real-time Motion Tracking of Freely Moving *Caenorhabditis elegans* via 2-axis Piezo Stage

HAIWEN LI^{1,5}, LIANG SHAN^{2,5}, SHUXIANG DONG², LOUIS TAO^{3,4} AND HENG MAO^{1,*}

¹ LMAM, School of Mathematical Sciences, Peking University, Beijing 100871, China

² College of Engineering, Department of Materials Science and Engineering, Peking University, Beijing 100871, China

³ Center for Bioinformatics, National Laboratory of Protein Engineering and Plant Genetic Engineering, School of Life Sciences, Peking University, Beijing 100871, China

⁴ Center for Quantitative Biology, Peking University, Beijing 100871, China

⁵ These authors contributed equally to this work

*heng.mao@pku.edu.cn

Abstract: This paper has fully investigated real-time motion tracking of freely moving *Caenorhabditis elegans* for the study of simultaneous behavioral and neural activities under the self-developed fluorescence microscope. In the past few years, step motor based and DC motor based 2-axis translation stages have been reported in most worm tracking systems. However, since the accuracy of single motion step is limited and the entire tracking loops are short of adaptivity, these motion stages can't provide the desired performances during the worm tracking and microscopic imaging. Therefore, we have alternatively implemented a 2-axis piezo stage and presented a hierarchical controlling and tracking strategy based on it. This strategy consists of the basic one for single motion step and the upper one for motion tracking loops. In the basic one, a closed-loop model for the motion response of each axis piezo stage has been characterized and determined, and a look-up table of optimized PID parameters in different axes, different positions and different steps has been established for real-time motor control. In the upper one, temporal multiplexing based tracking has been given to enhance the execution efficiency and adaptivity in the tracking loops. By analytically representing the real worm motion trace, a trace-simulated tracking experiment has been carried out to quantitatively evaluate the tracking performances, and the superiority of our strategy has been demonstrated. According to this strategy, the real-time worm tracking can be within rapid response, all-time high accuracy and smoothness.

© 2016 Optical Society of America

OCIS codes: (170.3880) Medical and biological imaging; (100.4999) Pattern recognition, target tracking; (110.4153) Motion estimation and optical flow.

References and links

1. C. Stauffer and W. E. L. Grimson, "Learning patterns of activity using real-time tracking," *IEEE Transactions on Pattern Analysis and Machine Intelligence* **22**(8), 747-757 (2000).
2. J. Krumm, S. Harris, B. Meyers, B. Brumitt, M. Hale, and S. Shafer, "Multi-camera multi-person tracking for EasyLiving," in *Visual Surveillance, 2000. Proceedings. Third IEEE International Workshop on (IEEE, 2000)*, 3-10.
3. C. Zimmer, E. Labruyere, V. Meas-Yedid, N. Guillen, and J. C. Olivo-Marin, "Segmentation and tracking of migrating cells in videomicroscopy with parametric active contours: a tool for cell-based drug testing," *IEEE Trans Med Imaging* **21**(10), 1212-1221 (2002).
4. J. W. Hsieh, S. H. Yu, Y. S. Chen, and W. F. Hu, "Automatic Traffic Surveillance System for Vehicle Tracking and Classification," *IEEE Transactions on Intelligent Transportation Systems* **7**(2), 175-187 (2006).
5. X. Yu, H. W. Leong, C. Xu, and Q. Tian, "Trajectory-Based Ball Detection and Tracking in Broadcast Soccer Video," *IEEE Transactions on Multimedia* **8**(6), 1164-1178 (2006).
6. M. C. Hu, M. H. Chang, J. L. Wu, and L. Chi, "Robust Camera Calibration and Player Tracking in Broadcast Basketball Video," *IEEE Transactions on Multimedia* **13**(2), 266-279 (2011).
7. X. Zhou, L. Xie, Q. Huang, S. J. Cox, and Y. Zhang, "Tennis Ball Tracking Using a Two-Layered Data Association Approach," *IEEE Transactions on Multimedia* **17**(2), 145-156 (2015).

8. Y. L. Chen, B. F. Wu, H. Y. Huang, and C. J. Fan, "A Real-Time Vision System for Nighttime Vehicle Detection and Traffic Surveillance," *IEEE Transactions on Industrial Electronics* **58**(5), 2030-2044 (2011).
9. S. Sivaraman and M. M. Trivedi, "Looking at Vehicles on the Road: A Survey of Vision-Based Vehicle Detection, Tracking, and Behavior Analysis," *IEEE Transactions on Intelligent Transportation Systems* **14**(4), 1773-1795 (2013).
10. T. Yang, F. Chen, D. Kimber, and J. Vaughan, "Robust People Detection and Tracking in a Multi-Camera Indoor Visual Surveillance System," in *2007 IEEE International Conference on Multimedia and Expo (IEEE, 2007)*, pp. 675-678.
11. W. Choi, C. Pantofaru, and S. Savarese, "A general framework for tracking multiple people from a moving camera," *IEEE Trans Pattern Anal Mach Intell* **35**(7), 1577-1591 (2013).
12. R. Umamaheshwaran, W. Bijker, and A. Stein, "Image Mining for Modeling of Forest Fires From Meteorat Images," *IEEE Transactions on Geoscience and Remote Sensing* **45**(1), 246-253 (2007).
13. A. Benavoli, L. Chisci, and A. Farina, "Tracking of a Ballistic Missile with A-Priori Information," *IEEE Transactions on Aerospace and Electronic Systems* **43**(3), 1000-1016 (2007).
14. O. Debeir, P. Van Ham, R. Kiss, and C. Decaestecker, "Tracking of migrating cells under phase-contrast video microscopy with combined mean-shift processes," *IEEE Trans Med Imaging* **24**(6), 697-711 (2005).
15. A. M. Leifer, C. Fang-Yen, M. Gershow, M. J. Alkema, and A. D. Samuel, "Optogenetic manipulation of neural activity in freely moving *Caenorhabditis elegans*," *Nat Methods* **8**(2), 147-152 (2011).
16. F. B. Shipley, C. M. Clark, M. J. Alkema, and A. M. Leifer, "Simultaneous optogenetic manipulation and calcium imaging in freely moving *C. elegans*," *Front Neural Circuits* **8**, 28 (2014).
17. J. Ben Arous, Y. Tanizawa, I. Rabinowitch, D. Chatenay, and W. R. Schafer, "Automated imaging of neuronal activity in freely behaving *Caenorhabditis elegans*," *J Neurosci Methods* **187**(2), 229-234 (2010).
18. B. J. Piggott, J. Liu, Z. Feng, S. A. Wescott, and X. Z. Xu, "The neural circuits and synaptic mechanisms underlying motor initiation in *C. elegans*," *Cell* **147**(4), 922-933 (2011).
19. S. Faumont, G. Rondeau, T. R. Thiele, K. J. Lawton, K. E. McCormick, M. Sottile, O. Griesbeck, E. S. Heckscher, W. M. Roberts, C. Q. Doe, and S. R. Lockery, "An image-free opto-mechanical system for creating virtual environments and imaging neuronal activity in freely moving *Caenorhabditis elegans*," *PLoS One* **6**(9), e24666 (2011).
20. M. Zheng, P. Cao, J. Yang, X. Z. Xu, and Z. Feng, "Calcium imaging of multiple neurons in freely behaving *C. elegans*," *J Neurosci Methods* **206**(1), 78-82 (2012).
21. S. Kato, H. S. Kaplan, T. Schrodell, S. Skora, T. H. Lindsay, E. Yemini, S. Lockery, and M. Zimmer, "Global brain dynamics embed the motor command sequence of *Caenorhabditis elegans*," *Cell* **163**(3), 656-669 (2015).
22. J. P. Nguyen, F. B. Shipley, A. N. Linder, G. S. Plummer, M. Liu, S. U. Setru, J. W. Shaevitz, and A. M. Leifer, "Whole-brain calcium imaging with cellular resolution in freely behaving *Caenorhabditis elegans*," *Proc Natl Acad Sci U S A* **113**(8), E1074-1081 (2015).
23. V. Venkatachalam, N. Ji, X. Wang, C. Clark, J. K. Mitchell, M. Klein, C. J. Tabone, J. Florman, H. Ji, J. Greenwood, A. D. Chisholm, J. Srinivasan, M. Alkema, M. Zhen, and A. D. Samuel, "Pan-neuronal imaging in roaming *Caenorhabditis elegans*," *Proc Natl Acad Sci U S A* **113**(8), E1082-1088 (2015).
24. S. Dong, "Review on Piezoelectric, Ultrasonic, and Magnetoelectric Actuators," *Journal of Advanced Dielectrics* **02**(01), 1230001 (2012).
25. Galil user manual, "man_21x2_21x3," http://www.galil.com/download/manual/man_21x2_21x3.pdf.
26. T. Yamamoto and S. L. Shah, "Design of a Performance-Adaptive PID Controller," in *2007 IEEE International Conference on Networking, Sensing and Control (IEEE, 2007)*, pp. 547-552.
27. W. Liang, K. K. Tan, S. Huang, L. P. Pham, H. Y. Lim, and C. W. Gan, "Control of a 2-DOF ultrasonic piezomotor stage for grommet insertion," *Mechatronics* **23**(8), 1005-1013 (2013).
28. S. Bi, L. Wang, Y. Zhao, and M. Deng, "Operator-based robust control for nonlinear uncertain systems with unknown backlash-like hysteresis," *International Journal of Control, Automation and Systems* **14**(2), 469-477 (2016).

1. Introduction

Motion tracking is an essential technique required in numerous real-time imaging applications[1-5]. In the tracking loop, dynamic image acquisition and processing have been done frame by frame, and the objects could be recognized immediately from the processing, as well as their regions, locations and other characteristics. After image processing the tracking might be correspondingly executed step by step in different ways.

For tracking under the macroscopic imaging, such as the eagle eye system in sport matches [5-7], the traffic surveillance system [4,8,9], the indoor person-tracking system [2,10,11] and etc, multiple cameras are involved for different viewpoints and each field of view (FOV) are moving fast by camera holder to capture the object(s).

For tracking under the telescopic imaging and remote imaging, such as the security monitoring, environmental monitoring [12], aircraft navigation, trajectory tracking [13] and etc, a very large FOV are usually given which doesn't need to change. In this way,

objects in the field are mainly in small size and can be treated as rigid bodies.

For tracking under the microscopic imaging, there are many additional troubles. Such as the depth of field (DOF) is strictly in few microns, the object is sometimes full of FOV, and the motion dynamic range is large. In the case of tracking the cell lifetime, shape and migration, if such cell grows and moves slowly and has the simplex body shape, it could be easily recognized from the fixed FOV [3,14], otherwise we should calculate its movement and decide to compensate the motion increments of sample by 2-Axis automated translation stage (ATS).

In this paper, we are tracking the freely moving *Caenorhabditis elegans* for the study of simultaneous behavioral and neural activities. As imagined, non-invasive imaging to the untethered model organisms is arguably the ultimate step in the analysis of neuronal function. Because the body size of *C. elegans* is around 1 mm, practical worm tracking can be only implemented in the following procedures. We calculate the position of neural region of interest (ROI) of worm from the locomotion and behavior imaging (LBI) and/or the neural calcium imaging (NCI), and compensate its interframe vertical and horizontal offsets by 2-axis ATS as fast as possible to guarantee the ROI always centering in the FOV of NCI.

As doing the optogenetic manipulation of freely moving *C. elegans* in single neuron or few neurons, motion tracking does not need to accurately recenter ROI in the FOV of NCI [15,16]. In this situation, calculating the centroid of worm region from LBI could be enough for motion compensation. Other researches for imaging the activities of neurons, neural circuit even pan-neuronal region, offsets of interframe could be estimated directly from NCI by feature extraction and pattern recognition [17-23]. To overcome the defocus problem during tracking, some of them distinguished the volume position from z-stack images [22,23].

Noticing the spatial resolution of NCI is usually ten times higher than the resolution of LBI, 2-axis motion compensation must be in high accuracy, rapid response and long-term smooth. Rapid response could decrease the motion interval and step, and smoothness could eliminate the blurring and enhance the spatial resolution. In the past few years, step motor based and DC motor based 2-axis translation stages have been reported in most worm tracking systems. However, since the accuracy of single motion step is limited and the entire tracking loops are short of adaptivity, these motion stages can't provide the desired performances during the worm tracking and microscopic imaging. And due to the unknown motion increments were involved in the calculated increments, it is impossible to quantitatively evaluate the tracking performances in principle.

This paper aims to alternatively implement a 2-axis piezo stage and propose a hierarchical controlling and tracking strategy based on it. This strategy consists of the basic one for single motion step and the upper one for motion tracking loops. In the basic one, a closed-loop model for the motion response of each axis piezo stage has been characterized and determined, and a look-up table of optimized PID parameters in different axes, different positions and different steps has been established for real-time motor control. In the upper one, temporal multiplexing based tracking has been given mainly to command 2-axis motion individually, increase the frame rate of image acquisition and processing and etc. By analytically representing the real motion trace of worm ROI, a trace-simulated tracking experiment has been carried out to quantitatively evaluate the tracking performances. Finally, the superiority of our tracking strategy has been demonstrated both in trace-simulated tracking experiment and real tracking experiment.

The paper is organized as follows. A self-developed *C. elegans* neural circuit tracking microscope with 2-axis piezo stage has been introduced in section 2. In section 3 and 4, strategies for optimizing the performances in single motion step and tracking loops have been given. Section 5 gives the trace-simulated tracking experiment and results. And the real motion tracking experiment of *C. elegans* has been finally presented in section 6.

2. Self-developed Tracking Microscope System

For *C. elegans* LBI and NCI system, as shown in Fig. 1, we used a 2-axis piezo stage (motor @Nanomotion, controller @GALIL, travel in 100mm, grating resolution in 100nm) holding a customized fused silica glass dish (inner diameter 60 mm). Worm was crawling on the top surface of 3mm agarose plate in the dish. In the LBI imaging, as shown in Fig. 2, 200 fibers coupled from two LED sources were fixed into a 70 degree reflected ring illuminator, and dark field images of the worm's locomotion and behavior were recorded through the agarose layer and a zooming lens (@Navitar, 0.7x-4.5x). In the NCI imaging, the 488nm and 561nm illumination were provided by two Laser modules (@Coherent, OBIS FP) and fluorescent images of the worm's neural activities (expressed both calcium indicator, GCaMP6s and red fluorescent protein, RFP) were recorded under different exposure timing from LBI based on the FPGA synchronization through a 20X objective without immersion (@Zeiss, working distance 1.2mm, N.A.~0.7) and other relay optics into two emission band paths. A high-speed industrial CMOS camera (@Dalsa, Falcon2, 4M) for LBI (~5ms exposure) and two sCMOS cameras (@Hamamatsu, Flash 4.0, 4M) for NCI (~5ms exposure) were employed, respectively.

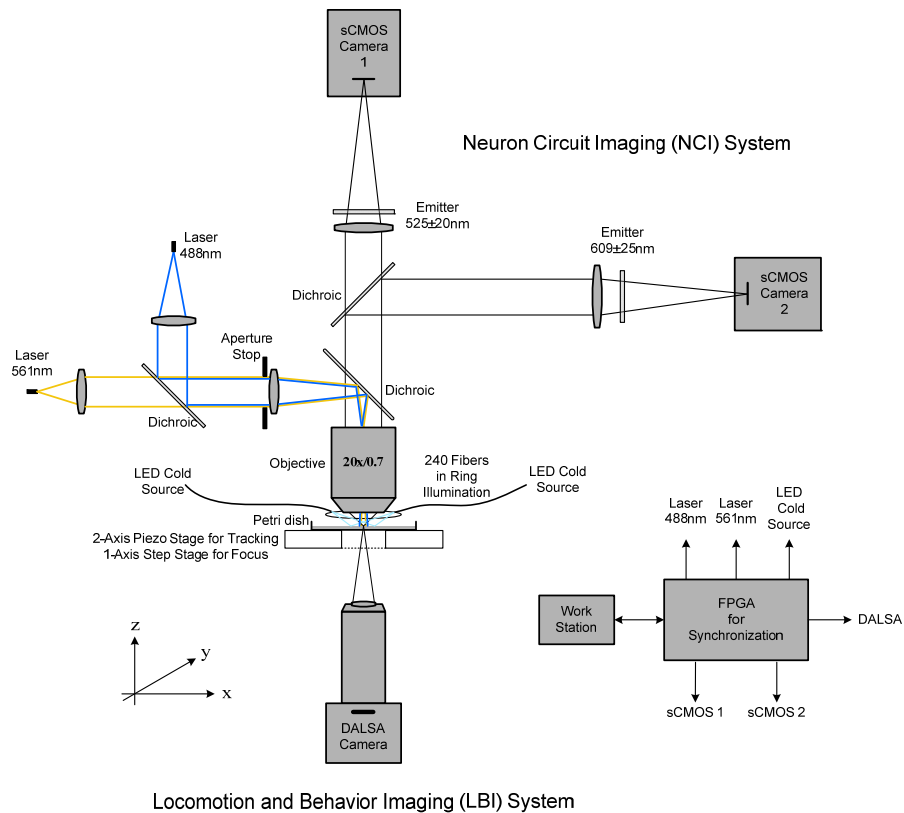


Fig. 1. Self-developed tracking microscope for freely moving *C. elegans*.

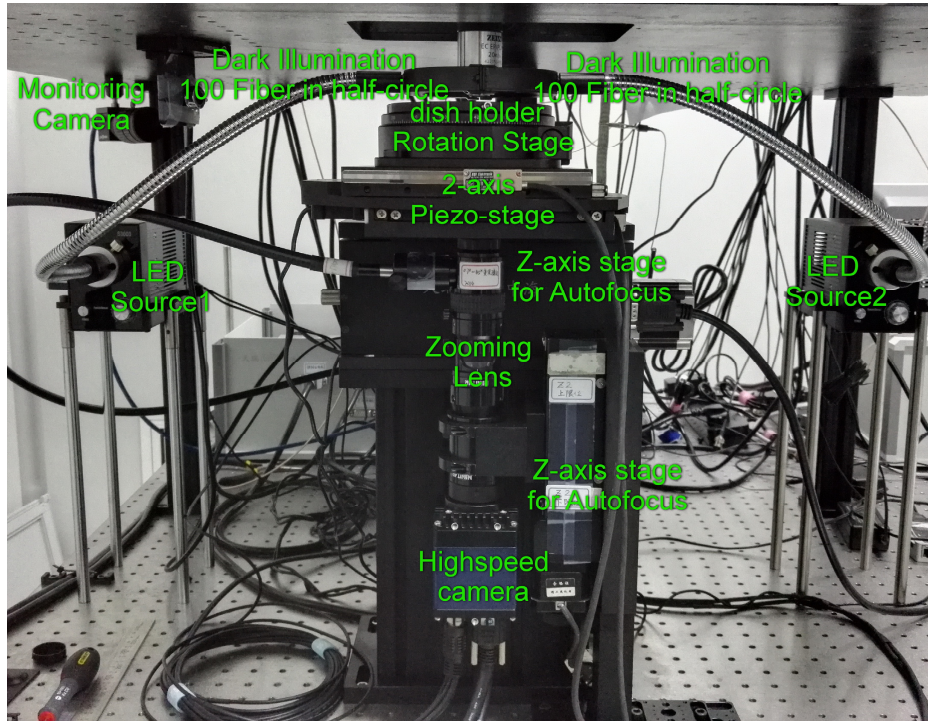


Fig. 2. Layout of locomotion and behavior imaging (LBI) system.

From the experimental knowledge, the wild type worm is in 0.8~1.5mm's long and 70-100um's wide. Moderate speed of its freely moving is 200~300um/s.

In the system, the sampling in LBI is 4.74um/pixel, and the sampling in NCI is 0.45um/pixel. Full FOV of LBI is 2432x1728 and full FOV of NCI is 2048x2048. Calculation of worm ROI position costs nearly 5ms per frame using a self-developed graphical user interface (GUI) written by QT in C++ and OpenCV and OpenGL to real-time display. Calculation errors depends on different algorithms in LBI and NCI normally less than 2 pixels and 1 pixel, respectively.

Before the implementation of motion compensation, three main types of motor (step motor, DC motor, piezoelectric motor) were taken into consideration, and we finally selected the piezoelectric motor to build the 2-axis stage due to it has such advantages as high resolution, high accuracy, high power density and low electromagnetic effects [24]. On the other side, the controlling complexity of piezoelectric motor is quite high and the motion performance needs to be optimized in-situ system.

3. Theory and Strategy

For the worm motion tracking, optimizations would be desired in two hierarchies. The basic hierarchy is inside the single motion compensation step, where the stage controller drives two piezoelectric motors to individually complete the command motion step (CMS) in closed-loop. And the upper hierarchy is in the motion tracking loop, where the image acquisition, motion calculation and motion compensation execute in sequence. In this section, models of these two hierarchies are given.

3.1. Motion Tracking Loop Model

After the k -th image acquisition and motion calculation, the position of worm ROI center has been obtained as (x_k, y_k) in the image plane. Then, the k -th motion compensation will be

executed as

$$\begin{pmatrix} H_k - H_{k-1} \\ V_k - V_{k-1} \end{pmatrix} = -M^{-1} \begin{pmatrix} x_k - x^* \\ y_k - y^* \end{pmatrix} + \begin{pmatrix} \mathcal{E}_H^k \\ \mathcal{E}_V^k \end{pmatrix} \quad (1)$$

where (H, V) is the position in 2-axis stage coordinates, (x, y) is the position in image detector coordinates, (x^*, y^*) is the appointed point in image FOV, M is the imaging magnification and $(\mathcal{E}_H^k, \mathcal{E}_V^k)$ is the random motion errors of 2-axis motion limited by the closed-loop accuracy of piezo stage.

After the k -th motion compensation, the $(k+1)$ -th image acquisition and motion calculation will be experienced and the position of ROI center (x_{k+1}, y_{k+1}) will be

$$M^{-1} \begin{pmatrix} x_{k+1} - x_k \\ y_{k+1} - y_k \end{pmatrix} = \begin{pmatrix} p_k - p_{k-1} \\ q_k - q_{k-1} \end{pmatrix} + \begin{pmatrix} H_k - H_{k-1} \\ V_k - V_{k-1} \end{pmatrix} \quad (2)$$

where (p, q) is the position of ROI center in the petri dish coordinates. And assume (p, q) , (H, V) and (x, y) be mutually paralleled in idealized case.

Substitute Eq. (1) into Eq. (2), we get

$$M^{-1} \begin{pmatrix} x_{k+1} - x^* \\ y_{k+1} - y^* \end{pmatrix} = \begin{pmatrix} p_k - p_{k-1} \\ q_k - q_{k-1} \end{pmatrix} + \begin{pmatrix} \mathcal{E}_H^k \\ \mathcal{E}_V^k \end{pmatrix} \quad (3)$$

This equation indicates that the vertical and horizontal offsets are basically dominated in latest motion increments of worm during the last motion tracking. That is why it is hard to evaluate the tracking performances from these offsets sequences. In addition, considering the motion increments are changing in continuous and limited to $20\mu\text{m}@15\sim 20\text{Hz}$, we firmly insist to do the motion compensation without any predictions in our system, defined as the unbiased motion compensation.

Due to the piezo stage is susceptible to the external factors, such as load, abrasion, local surface irregularities of ceramic and etc, it doesn't have high repeatability and must be controlled in closed-loop. Therefore, proper PID parameters and control strategies need to be optimized for the in-situ 2-axis stage.

3.2. Single Motion Closed-loop Model

For the single step motion compensation, the piezo stage controller operated in closed-loop by @Galil motion control card (MCC) [25] functionally involves three parts: PID Control, Motor Response and Negative Feedback, as shown in Fig. 3. In this closed-loop, there are four process variables $a(n)$, $e(n)$, $W(n)$ and $\Delta(n)$ can be readout and six parameters can be reset via the controller software in real-time.

Generally, the horizontal and vertical axes of piezo stage are fixed together and controlled by the same MCC. In this way, PID control acts the same function on these two axes, but their Motor Responses are apparently different. Motor Response is probably a multi-factor affected model basing on the piezoelectric motor uniqueness, surface friction, related mechanism and material properties. In this section, taking the horizontal axis of piezo stage for example, its closed-loop model has been characterized and determined.

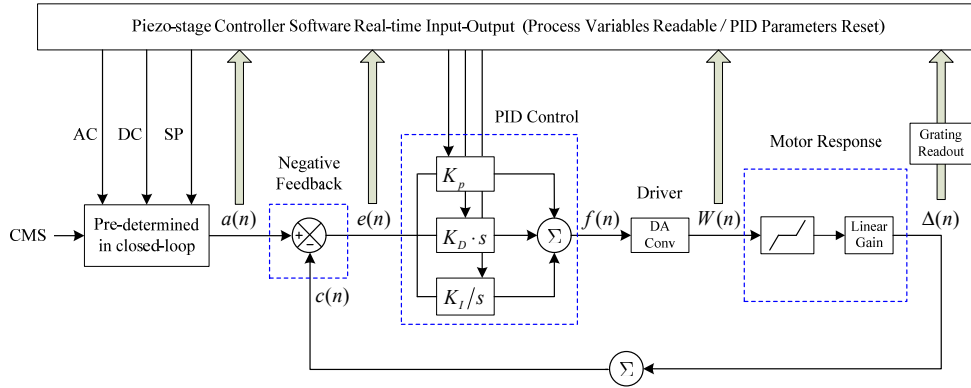


Fig. 3. Schematic of closed-loop motion model. $a(n)$: pre-determined position (um); $e(n)$: actual PID input (um); $f(n)$: digital PID output (um); $W(n)$: analog driving voltage (mV); $\Delta(n)$: actual increment (um); $c(n)$: actual position (um).

In the closed-loop, once the k-th CMS is given by $-M^{-1}(x_k - x^*, y_k - y^*)$ from Eq. (1), the referring position sequence $a(n)$ can be pre-determined by three adjustable parameters, acceleration speed (AC), deceleration speed (DC) and constant speed (SP) according to the Acceleration-Constant-Deceleration (ACD) model. Fig. 4 gives the actual $a(n)$ from software readout and simulated $a(n)$ from determined CMS and ACD model calculation. From $a(n)$ to the PID input $e(n)$, a negative feedback of actual position $c(n)$ from integration of $\Delta(n)$ is experienced.

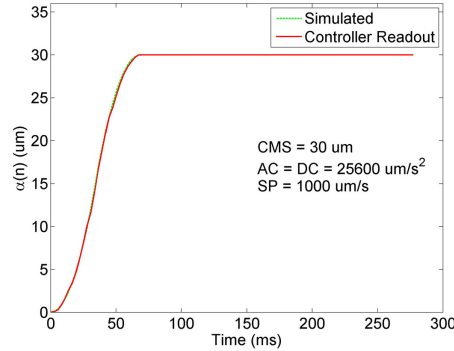


Fig. 4. Simulation of $\alpha(n)$ from determined CMS and parameters AC, DC, SP.

In the PID Control, three other adjustable parameters K_p , K_I and K_D , which represent the proportional, integral, derivative portion of PID output, are involved. And the n-th PID output $f(n)$ is

$$f(n) = K_p \cdot e(n) + K_I \cdot \sum_{i=0}^n e(i) + K_D \cdot [e(n) - e(n-1)] \quad (4)$$

After the PID output, the MCC uses a DA circuit to convert $f(n)$ into analog driving voltage $W(n)$ by a linear factor μ . Simulation of $W(n)$ from the readout $e(n)$ has been done to fit μ and validate the model. An example of readout $W(n)$ and simulated $W(n)$ as $K_p=8$, $K_I=2$, $K_D=2.5$ and fitted $\mu=1.2145$ mV/um, is shown in Fig. 5.

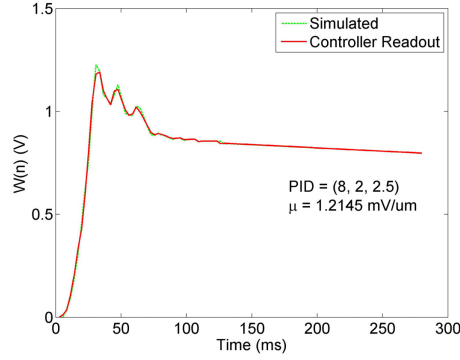


Fig. 5. Simulation of $W(n)$ from determined $e(n)$ and parameters K_p, K_i, K_d, μ .

In the Motor Response, referring to [26,27] the discrete transfer function of piezoelectric motor from driving voltage $W(n)$ to actual motion increment $\Delta(n)$ has been treated as an accumulating linear process and derived as

$$\Delta(n) = \frac{\lambda}{T} \sum_{m=0}^n e^{-m \frac{\Delta t}{T}} \cdot W(n-m) \quad (5)$$

where three inner parameters λ, T and Δt denote the response gain, time constant and time interval of loop, respectively. Moreover, considering the driving force of piezoelectric motor needs to overcome the static friction before it does work on the slider and the intrinsic hysteresis and creep of piezoelectric materials [28] would postpone the motion response, we attempt a thresholding process to approximate this nonlinear influence on $W(n)$ as follows

$$\tilde{W}(n) = \begin{cases} \text{sign}[W(n)] \cdot [|W(n)| - W_T], & \text{if } |W(n)| > W_T \\ 0, & \text{otherwise} \end{cases} \quad (6)$$

where W_T is a threshold of $W(n)$. $W(n)$ in Eq. (5) can be modified by $\tilde{W}(n)$. $a(n), e(n)$ and $W(n)$ can be directly readout from MCC, while $\Delta(n)$ is experienced an access of grating module and a returning delay before readout, as shown in Fig. 3. That would induce an additional sampling delay between $W(n)$ and $\Delta(n)$.

Four inner parameters $\lambda, T, \Delta t$ and W_T have been fitted over a large number of trials from the readout $W(n)$ to the readout $\Delta(n)$. Fig. 6 shows the simulation of $\Delta(n)$ from the known $W(n)$ and approximated model in Eq. (5) and Eq. (6). Fitting errors mainly come from the simplification of our model.

After above discussions, the entire closed-loop model for single axis piezo stage has been given, which includes five inner parameters $\mu, \lambda, T, \Delta t$ and W_T , and six adjustable parameters $K_p, K_i, K_d, AC, DC, SP$. These six parameters can be reset in real-time and we call them as PID parameters in following context. Fig. 7 is an example of the entire closed-loop simulation as $CMS=30\mu m, AC=DC=25600\mu m/s^2, SP=1000\mu m/s, K_p=8, K_i=2, K_d=2.5$. The actual position $c(n)$ integrated by $\Delta(n)$ from MCC readout and the simulated $c(n)$ from the entire closed-loop model have high consistency and the normalized correlation is more than 0.95. Comparing the fitting errors in Fig. 6 and Fig. 7, it shows

that $c(n)$ output from the entire model effectively eliminated the fitting errors caused by Motor Response.

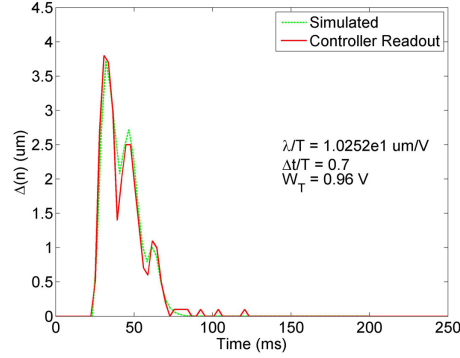


Fig. 6. Simulation of $\Delta(n)$ from determined $W(n)$ and parameters λ , T , Δt and W_T .

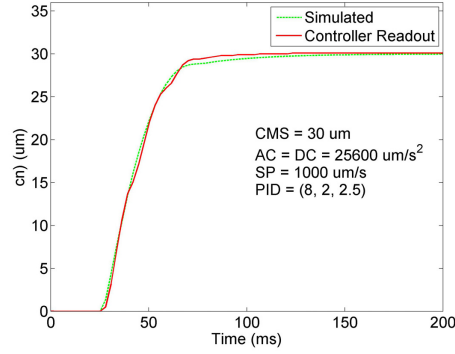


Fig. 7. Entire closed-loop simulation of $c(n)$.

3.3. Optimal Strategy in Single Motion Closed-loop

From practical experiments, the actual motion traces $c(n)$ for the single motion compensation are definitely different under the different CMSs, different axes, different axis positions, or different PID parameters. It drives us to implement an optimal strategy to adaptively control the 2-axis piezo stage in every single motion closed-loop. Otherwise, 2-axis piezo stage couldn't perform in good working state, even worse than the performance of step motor stages.

(1) Adaptively setting proper PID parameters for the different axes, positions and CMSs.

In consideration of high real-time requirement, we establish a look-up table of proper PID parameters for different axes, positions and CMSs from 5μm to 60μm, as shown in Table 1&2. And for other value of CMS, nearest interpolation can be adopted.

To avoid occupation of another thread for PID control in PC, we implement the above adaptive PID control on @Galil MCC and program it on the ROM of the controller to execute in endless loop.

(2) Giving a startup threshold for motion compensation.

If the CMS is less than few microns, sometimes it may not be generated from the worm moving but from the ROI calculation errors (in pixel-level). On the other hand, few microns CMS may also cause a long time response for piezo stage in closed-loop (as discussed later in section 4.1, Table 1&2). Therefore, giving a startup threshold for motion compensation is necessary for long-term tracking smoothness.

3.4. Optimal Strategy in Motion Tracking Loop

In the motion tracking loop, we proposed:

- (1) to increase the frame rate of image acquisition and motion calculation (called motion sampling in context) ;
- (2) to do the 2-axis motion compensation individually.

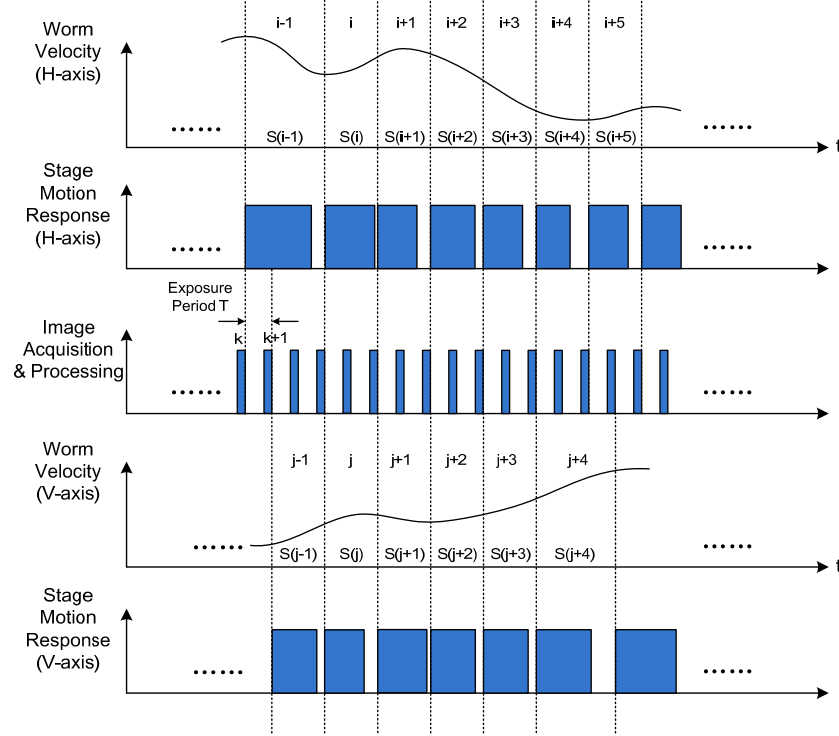


Fig. 8. Optimal tracking timing for two axes working individually.

In common compensation mode, 2 axes start the motion at the same time after the last 2 axes motions are all finished and the new motion calculation is complete. Considering a special case that the current H-axis offset is much bigger than the V-axis offset, the V-axis stage may wait for a while to do the next compensation. For enhancing the execution efficiency and shortening the motion interval, the frame rate of motion sampling should be increased and two axes should work independently as

$$\begin{aligned}
 M^{-1}(x_{i+1} - x^*) &= (p_i - p_{i-1}) + \varepsilon_H \\
 M^{-1}(y_{j+1} - y^*) &= (q_j - q_{j-1}) + \varepsilon_V
 \end{aligned} \tag{7}$$

where i and j are the indices of motion response on H-axis and V-axis, and two axes motions are not in the same interval depending on the different CMSs.

As illustrated in Fig. 8, when the motion sampling (the third line timing) is in higher frame rate, 2-axis motion responses are all in better duty cycle, where $S(i) = p_i - p_{i-1}$ and $S(j) = q_j - q_{j-1}$ integrated by worm velocity along the response period (between two neighboring dashed).

4. Determination of Practical Parameters

4.1. Proper PID parameters for the different axes, positions and CMSs

As proposed in section 3.3, proper PID parameters for the different axes, positions and CMSs need to be given adaptively by the controller to guarantee the piezo stage working in good performance during the motion tracking. In this paper, the tracking performances for freely moving *C. elegans* are concerned with the following three respects, response speed, accuracy and long-term smoothness. Therefore, the objective function about the actual motion trace $c(n)$ in single motion closed-loop can be

$$E = \alpha \cdot T_s + \beta \cdot |E_r| + \gamma \cdot S \quad (8)$$

where T_s is the time duration before the stage gets stable, E_r is the position error between $a(n)$ and $c(n)$ when the stage gets stable, and S is a measure of smoothness of $c(n)$. The weight factors α , β , γ in different unit can make three items unitless. And the first and second items are supposed to be more important. In practice, we approximately estimated α , β , γ with the maximum errors we can tolerate and set them as normalized weights, $(1.0 \cdot 1/100\text{ms})$, $(0.8 \cdot 1/1\mu\text{m})$ and $(0.3 \cdot 1/200\mu\text{m})$, respectively. Based on this evaluation, we can find different optimized PID parameters for the different axes, positions and CMSs by model. After that, we manually adjusted PID parameters in only a small change based on the actual stage response.

Table 1 and Table 2 are the final results of proper PID parameters for the different axes, positions and CMSs. In the tables, CMS is considered from 5um to 60um which are much related to the worm tracking situation. And the optimal response time for different CMSs, axes, and positions are also given in the column of mean and std (standard deviation). And all these response time is in the range of 40~85ms indicating the special motion characteristics of piezoelectric motor other than step motor.

From the results, we investigated seven points uniformly on the H-axis's travel and seven points on the V-axis's travel, totally 49 positions for the analysis of response differences of different stage positions. As shown in Fig. 9, (a) and (b) are the H-axis response differences in CMS 10um and 20um, respectively; (c) and (d) are the V-axis response differences in CMS 10um and 20um, respectively. It can be seen that all differences are in small level (few ms) and become consistent while the CMS reaches to 20um. For this reason, we decide to ignore the influences of different stage positions in the strategy of adaptively setting PID parameters in motion tracking. Fig. 10 presents two PID parameters optimization results in actual motion trace $c(n)$ as CMS are 23.5um and 37.2um.

Table 1. Optimized PID Parameters for H-axis

Step (um)	P	I	D	AC/DC (um/s ²)	SP (um/s)	Response Time mean, std (ms)
5	5.5	4.0	3.5	12800	1000	59.63, 1.51
10	5.5	3.5	3.0	12800	1000	58.04, 4.09
20	6	2.845	3.0	20000	1000	57.92, 1.29
30	6.5	2.845	2.5	30000	1000	62.98, 1.42
40	7	2.845	2.5	50000	1000	58.12, 1.38
50	8	2.645	2.75	128000	2000	40.24, 3.02
60	8	2.5	2	256000	2000	36.61, 3.09

Table 2. Optimized PID Parameters for V-axis

Step (um)	P	I	D	AC/DC (um/s ²)	SP (um/s)	Response Time mean, std (ms)
5	6.5	4.0	3.5	25600	1000	73.18, 4.14
10	6.5	3.0	3.5	25600	1000	71.67, 3.22
20	6.5	2.45	3.5	25600	1000	78.04, 2.22
30	6.5	2.203	3.5	25600	1000	80.20, 2.42
40	7	2.325	3	51200	1000	70.20, 1.97
50	7	1.85	3.5	128000	1000	69.14, 1.87
60	7	1.85	3.5	200000	1500	64.53, 2.73

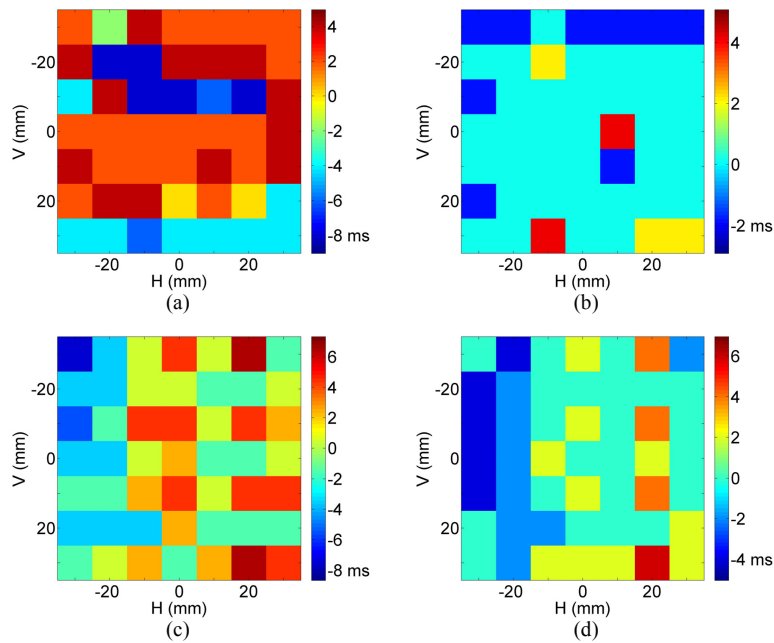


Fig. 9. Differences of response time for 7x7 positions on two-axis piezo stage in the same CMS. (a) Differences of response time of H-axis as CMS is 10um (mean value removed). (b) Differences of response time of H-axis as CMS is 20um (mean value removed). (c) Differences of response time of V-axis as CMS is 10um (mean value removed). (d) Differences of response time of V-axis as CMS is 20um (mean value removed).

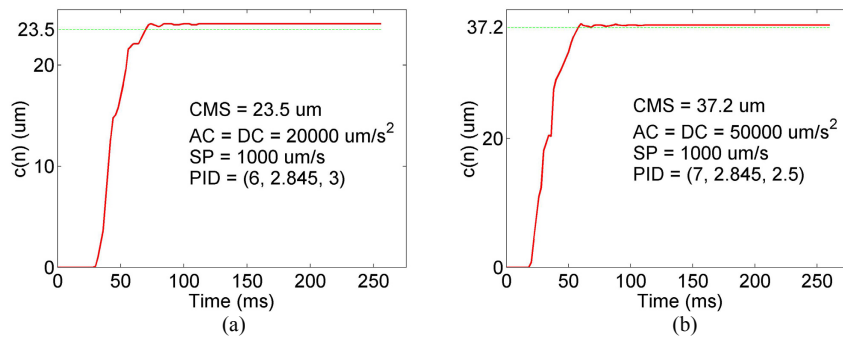


Fig. 10. PID parameters optimized results of $c(n)$ in H-axis. (a) CMS is 23.5um. (b) CMS is 37.2um.

4.2. Startup threshold for motion compensation

As seen in Table 1&2, time consumption of single motion step within few microns may cost more, and the actual trace can't perform well. Finally, we set the startup threshold of CMS as 3um, less than 1pixel in LBI and 7pixels in NCI. Any CMSs less than the threshold will not be executed and be treated as uncertain error. Even if the worm indeed moves in such short step, we can accumulate and capture it in next frame.

4.3. Optimal frame rate of motion calculation

As illustrated in Fig. 8, higher frame rate of motion calculation makes 2-axis piezo stage response faster and more continuous with fewer pauses. However, due to the exposure of LBI and NCI are in asynchronous, the total exposure duration of LBI will be limited to 200ms per second in order to provide enough fluorescent imaging of neuronal activities. In our system, single LBI costs 5ms in exposure. That means the maximum frame rate of LBI is 40Hz.

On the other side, Table 1 indicates the maximum motion response of H-axis is 65ms, and on V-axis is 85ms. Up to now, we need to further determine the optimal frame rate and quantitatively analyze its influences in our tracking system, over the range of 12 to 40Hz.

5. Evaluation of Tracking Performance

5.1. Practical method

In order to evaluate the performance of real-time motion tracking on freely moving *C. elegans*, the real trace of worm ROI moving and the actual trace of 2-axis piezo stage in the same coordinate should be all known. As shown in Eq. (7) and Fig. 8, the real trace of worm ROI moving during the real-time motion can be hardly obtained. Because not only the real motion increments of worm $(p_i - p_{i-1})$ and $(q_j - q_{j-1})$, but also the stage motion errors and the calculation errors are involved in the offset of $(x_{i+1} - x^*)$ and $(y_{j+1} - y^*)$.

Besides, it is infeasible to let MCC software real-time return the working state of two axes to see whether the axis completed latest motion response following the current motion sampling. Interference of concurrent threads in both-way communication with MCC and real-time image display and processing will dramatically break the tracking continuity in practice.

In this section, a trace-simulated tracking experiment has been proposed to quantitatively evaluate the tracking performance. At first, we analytically represented the real trace of worm ROI moving $(p(t), q(t))$ from the videos in non-tracking. Then 2-axis motion tracking was executed under the entire real trace known. This experiment saved the LBI and NCI image acquisitions and ROI calculations, and successfully avoided the interference of threads in real-time tracking. Moreover, calculation errors would be excluded from the tracking errors.

In this trace-simulated tracking experiment, assuming the 2-axis stage coordinates are identical with the petri dish coordinates, ε_H and ε_V can be presented as $(p_{i-1} - H_i)$ and $(q_{j-1} - V_j)$. Eq. (7) becomes

$$\begin{aligned} M^{-1}(x_{i+1} - x^*) &= p_i - H_i \\ M^{-1}(y_{j+1} - y^*) &= q_j - V_j \end{aligned} \tag{9}$$

As motion errors in closed-loop are limited to stage closed-loop accuracy (1um), Eq. (9) has the limitation as

$$\begin{aligned}
M^{-1}(x_{i+1} - x^*) &= p_i - p_{i-1} \\
M^{-1}(y_{j+1} - y^*) &= q_j - q_{j-1}
\end{aligned} \tag{10}$$

Expecting the entire actual trace of stage to approach the real trace of worm ROI moving on all positions and times as far as possible, motion tracking errors (MTE) should be evaluated in sufficient motion sampling and stage sampling for the position readout as following expressions.

$$\text{MTE}_1 = \sqrt{\frac{1}{N} \sum_{k=1}^N (p_k - H_k)^2 + (q_k - V_k)^2} \tag{11}$$

$$\text{MTE}_2 = \frac{1}{N} \sum_{k=1}^N \sqrt{(x_k - x^*)^2 + (y_k - y^*)^2} \tag{12}$$

$$\text{MTE}_3 = \sqrt{\frac{1}{N} \sum_{k=1}^N (p_{k-\Delta_H} - H_k)^2 + (q_{k-\Delta_V} - V_k)^2} \tag{13}$$

$$\text{MTE}_4 = \sqrt{\frac{1}{N} \sum_{k=1}^N P_{\text{real trace}}^2(H_k, V_k)} \tag{14}$$

where k is the time index of motion sampling and stage sampling, Δ_H and Δ_V are the averaged time of motion response in H-axis and V-axis, and $P_{\text{real trace}}(H_k, V_k)$ is perpendicular distance from (H_k, V_k) to the $(p(t), q(t))$.

Here, MTE_1 stands for the root of mean square (RMS) of total errors between the worm ROI current position and stage position. And referring to Eq. (9), MTE_2 is much similar to MTE_1 and can be used for evaluating real-time tracking errors. Due to the motion increment $(p_k - p_{k-1}, q_k - q_{k-1})$ dominates MTE_1 and MTE_2 , it is improper to evaluate the real-time motion compensation. MTE_3 stands for the averaged motion compensation errors between the stage aimed position and current position. Here, Δ_H and Δ_V indicates the tracking performance of response time. MTE_4 stands for the tracking trace errors between the analytical worm ROI moving curve and the discrete 2-axis stage curve.

5.2. Representation of worm ROI real trace

A large number of trials have been done to study the freely moving worm trajectories on both the spatial domain and temporal domain. ROI moving trace in temporal trajectory could be mainly separated into two intrinsic parts. One belongs to the target curve with low frequency components; another belongs to the body wiggling curve with higher frequency components. Both are continuous and smooth.

By applying the least square fitting of quadratic curve to the x-axis components $p(t)$ and y-axis components $q(t)$ of the real trace section (20 seconds, limited to the LBI FOV), respectively. We estimated the target curve $p_{\text{tar}}(t)$ and $q_{\text{tar}}(t)$ in analytical form. And the residual components from the real trace correspond to the body wiggling curve, as shown in Fig. 11.

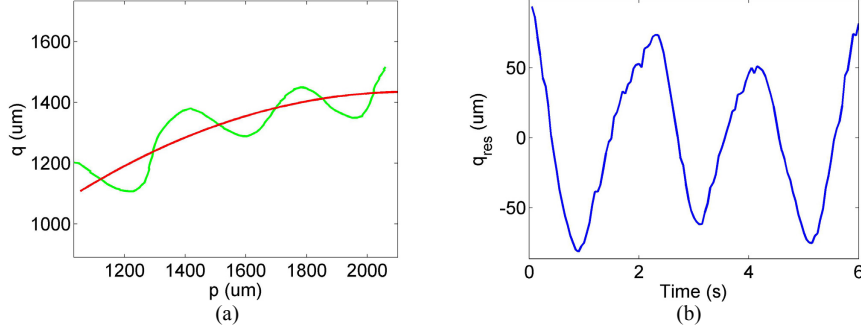


Fig. 11. Decomposition of the ROI real trace section. (a) ROI real trace in green curve and fitted target curve in red curve. (b) Residual time-variant y-axis components in blue curve.

Apparently, those residual components on x-axis and y-axis could be represented by some low order simple harmonic waves

$$\begin{aligned}
 p_{\text{res}}(t) &= a_0 + \sum_{w=1}^W a_k \cdot \cos(2\pi w f_0 t) + b_k \cdot \sin(2\pi w f_0 t) \\
 q_{\text{res}}(t) &= m_0 + \sum_{w=1}^W m_k \cdot \cos(2\pi w f_0 t) + n_k \cdot \sin(2\pi w f_0 t)
 \end{aligned} \tag{15}$$

where f_0 is the base frequency from the reciprocal of time duration of trace section, and parameters $\{a_0, a_1, \dots, a_W; b_1, \dots, b_W\}$ and $\{m_0, m_1, \dots, m_W; n_1, \dots, n_W\}$ could be fitted from the trace section.

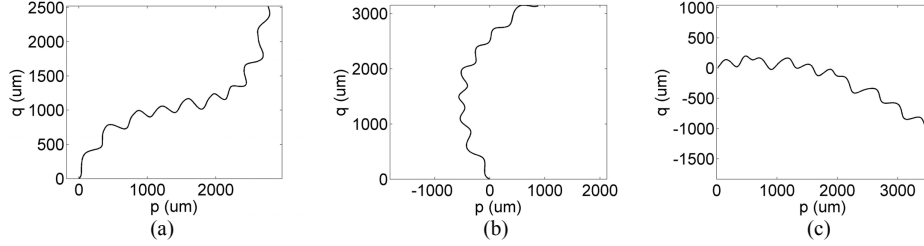


Fig. 12. Three typical trials of worm ROI trace by analytical representation.

By using above representation method, three typical trials of worm ROI real trace in 20 seconds freely moving (recording @20Hz) have been analytically reconstructed, as shown in Fig. 12. And the RMS of fitting errors in three trials are 5.06um, 5.70um, 6.25um, respectively, as the maximum order W is 8.

$$\begin{aligned}
 \hat{p}(t) &= p_{\text{tar}}(t) + p_{\text{res}}(t) \\
 \hat{q}(t) &= q_{\text{tar}}(t) + q_{\text{res}}(t)
 \end{aligned} \tag{16}$$

5.3. Trace-simulated worm tracking experiment

For the three analytical worm ROI traces, we carried out worm tracking experiments according to the optimal strategies in section 3 and optimal parameters in section 4 under the frame rates of motion sampling as 3, 4, 5, 6, 8, 10, 12, 15, 20, 24, 30, 40, 60, 120Hz and the stage sampling in all trials was 120Hz.

Tracking loop executed in k-th sequence (different motion sampling):

- (1) Readout current positions of 2-axis stage (H_k, V_k) at 120Hz;

- (2) Calculate current ROI real positions (p_k, q_k) from analytical trace;
- (3) Calculate current CMS $(p_k - H_k, q_k - V_k)$;
- (4) Communicate the H-axis stage to move CMS $(p_k - H_k)$. If H-axis is ready this CMS will be immediately response;
- (5) Communicate the V-axis stage to move CMS $(q_k - V_k)$. If V-axis is ready this CMS will be immediately response;
- (6) Wait for the end of current loop.

In the experiment, the initial stage position (H_1, V_1) was nearby the first position of real trace (p_0, q_0) and motion tracking lasted for 20 seconds. Fig. 13 indicates two stage motion traces of the first trial at 3Hz and 20Hz, respectively.

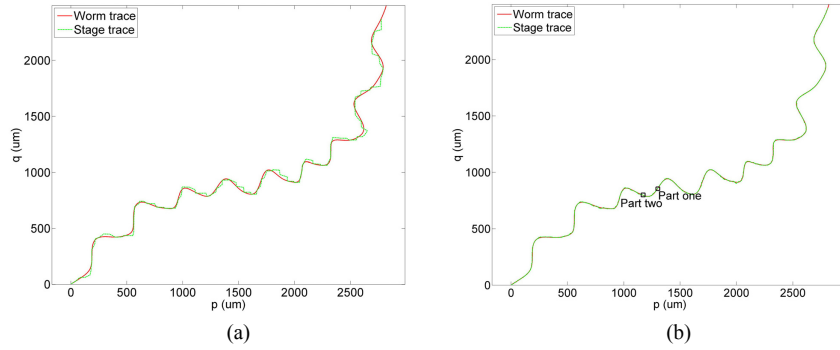


Fig. 13. Motion traces of first trial at different motion samplings. (a) 3Hz. (b) 20Hz.

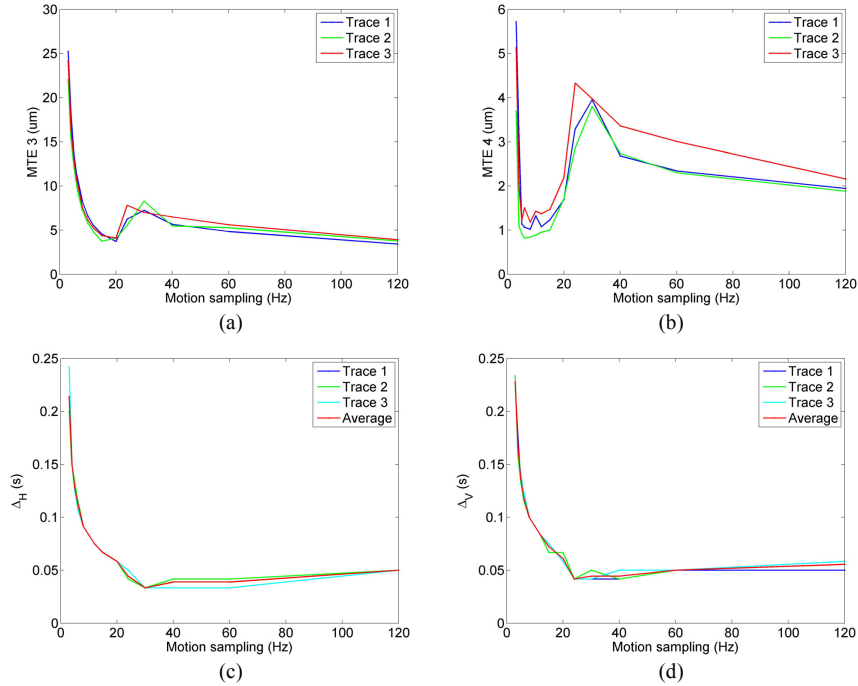


Fig. 14. Performances of different trials at different motion samplings. (a) Tracking errors MTE_3 . (b) Tracking errors MTE_4 . (c) Averaged motion response time in H-axis. (d) Averaged motion response time in V-axis.

5.4. Evaluation of tracking performances

After above experiment, 42 actual motion traces for three trials and 14 frame rate options have been acquired. The motion tracking errors were calculated by MTE_3 and MTE_4 in Fig. 14(a) and Fig. 14(b), where Δ_H and Δ_V have been estimated in Fig. 14(c) and Fig. 14(d) by maximum cross-correlation between the known trace and actual motion trace.

As presented in Fig. 14, for the first trial in 20Hz motion sampling, the tracking errors MTE_4 was 1.7 μm , and the Δ_H and Δ_V were 58.3ms and 66.7ms which were consistent with the optimized results in Table 1 and Table 2. It implied the effective fame rate of single axis motion is 16~17Hz. Referring to these results, the frame rate of motion sampling later in the real-time worm tracking would be optimized as 20Hz, allowing a little adjustment depending on the moving speed of worm.

Although the tracking errors in MTE_3 and MTE_4 were evaluated respectively in temporal domain and spatial domain, these two curves had the similar tendencies in decreasing from 3Hz to 20Hz, increasing from 20Hz to 30Hz, and decreasing again more than 30Hz. In order to clarify these distributions, we checked the trace details at different sampling frame rates.

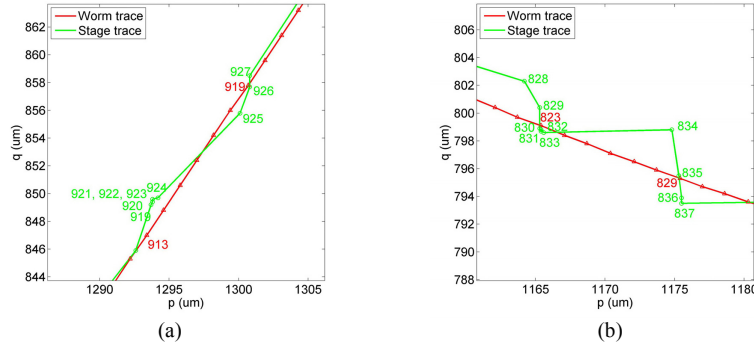


Fig. 15. Two parts of motion trace of the first trial at 20Hz motion sampling. (a) Enlarged part one of motion trace in Fig. 13(b). (b) Enlarged part two of motion trace in Fig. 13(b).

As illustrated in Fig. 15, the sampling points on real trace were uniformly spread but the stage readout points at 120Hz were partially gathered and partially sparse. In Fig. 15(a), points from 919-th to 924-th were nearly in a state of stagnation, and points from 924-th to 927-th were experienced a fast moving. Due to the two motion axes were controlled individually, when the frame rate rose to 20Hz, it is possible to see that one axis became getting start while another axis was still in situ, as shown in Fig. 15(b). This might cause the actual motion trace deviating from the real trace and consequently increased the tracking errors both in MTE_3 and MTE_4 , especially in MTE_3 .

Basing on the clues above, we attempt to interpret the distributions of MTE_3 and MTE_4 in Fig. 14(a) and Fig. 14(b).

[1] As the frame rate rising from 3Hz to 15Hz, MTE_3 and MTE_4 would be getting smaller due to the interval of motion compensation was shortening and two axes kept synchronous in most motion steps.

[2] As the frame rate rising from 20Hz to 30Hz or more, MTE_3 and MTE_4 would be increasing due to two axes became asynchronous in many motion steps, and the response time was approaching to the limitation, as illustrated in Fig. 14(c) and (d).

[3] As the frame rate rising to more than 40Hz, the period between two motion samplings was decreasing and the negative effect of asynchronous motions on MTE_3 and MTE_4 was reducing. However, due to the motion steps became smaller and bigger in alternating appearance, MTE_3 and MTE_4 could not decrease in a remarkable level and still more than the values at 20Hz. For example, for a distance of 30um, the H-axis will probably execute two steps of 15um and 15um at 20Hz, and 5um and 25um at 40Hz, the latter costs more response

time and introduces more errors in MTE_3 and MTE_4 .

In addition, the trace-simulated tracking experiment in the case of two axes motion in synchronous, according to Eq. (3), has also been done. While in every single motion step, the PID parameters still be optimized from the look-up table and set in real-time. Fig. 16 gave the tracking performances. By comparing with the Fig. 14, no obvious improvements have been found. And when the frame rate is less than 20Hz, it has demonstrated that the tracking errors from our tracking strategy would be smaller and more consistent in three trials.

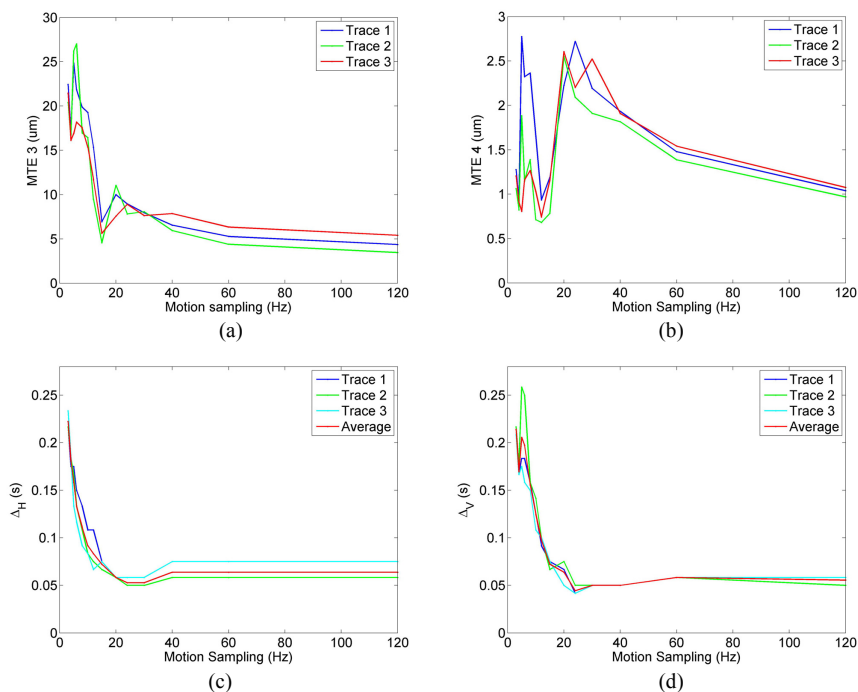


Fig. 16. Performances of different trials at different motion samplings in synchronous motion. (a) Tracking errors MTE_3 . (b) Tracking errors MTE_4 . (c) Averaged motion response time in H-axis. (d) Averaged motion response time in V-axis.

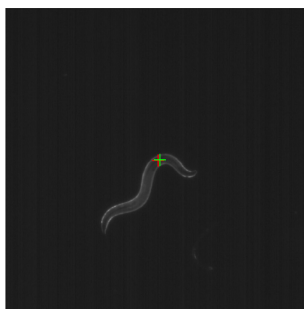


Fig. 17. Single frame in real-time worm tracking at 20Hz.

6. Real-time Tracking Experiments

In the real-time worm tracking experiment, the optimized strategies and parameters in section 3, 4 and 5 have been adopted. Because the moving traces for different worms at different times are inaccessible and unrepeatable, stage sampling would cause the interference with image processing and display threads perceived from the monitor, and high speed in motion sampling would limit the total exposure of NCI per second, the real-time tracking

experiments have been done without stage sampling and with motion sampling as 8Hz, 15Hz, 20Hz and 30Hz, respectively.

As described in section 3.1, the worm ROI center could be real-time calculated and located in the centerline coordinates. As shown in Fig. 17, the green cross and red cross indicated the real ROI center (x_k, y_k) and the FOV center (x^*, y^*) , respectively. Two axes were drove to move $-M^{-1}(x_k - x^*)$ and $-M^{-1}(y_k - y^*)$ via proper PID parameters if individual former motion was accomplished. By using the customized ring illumination, customized fused silica glass petri dish and agarose substrate, the worm LBI images acquired through the agarose layer and dish bottom are very desired to do the body segmentation and further image processing. Moreover, in our self-developed GUI two automatic tracking modes are provided, including Centroid Tracking and ROI Tracking. Once putting a single worm into the dish, the Centroid Tracking can work all the time, and ROI Tracking can work more than half an hour unless the worm was coiling or approaching to the dish edge.

For the real-time tracking, a large number of experiments were done in nearly 40 seconds for 5 individuals in every frame rate option. Comparing with the trace-simulated tracking experiment, not only worm motion increments $(p_i - p_{i-1})$ and $(q_j - q_{j-1})$ but also calculation errors $(\varepsilon_x, \varepsilon_y)$ from localization algorithm and motion errors $(\varepsilon_H, \varepsilon_V)$ were involved in image offset $(x_{i+1} - x^*)$ and $(y_{j+1} - y^*)$ in real-time tracking. Then Eq. (7) can be

$$\begin{aligned} M^{-1}(x_{i+1} - x^*) &= (p_i - p_{i-1}) + \varepsilon_x + \varepsilon_H \\ M^{-1}(y_{j+1} - y^*) &= (q_j - q_{j-1}) + \varepsilon_y + \varepsilon_V \end{aligned} \quad (17)$$

As discussed in Section 5.1, we can't return any state variables of two axes from MCC during the real tracking experiment. The only MTE we could calculate is the MTE_2 , which is the mean offset between ROI center and FOV center. As shown in Fig. 18, the mean image offsets decreased in average, which indicates the FOV center of NCI becoming closer to the ROI target and the variances somehow reflecting the robustness of our tracking strategy. Although the mean offset at 30Hz was smaller than 20Hz, the standard deviation at 30Hz is approximate two times than 20Hz. It implies that tracking will become unstable when the frame rate becomes more than 20Hz.

The video of long-term real-time tracking experiments can be seen at (<http://www.math.pku.edu.cn/teachers/maoh/TrackMicro.html>).

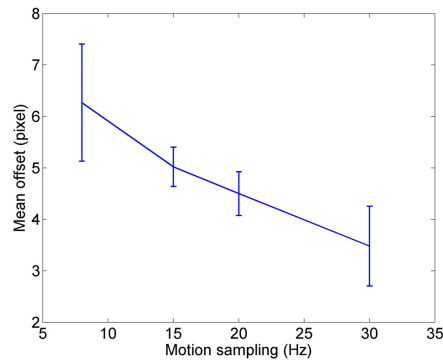


Fig. 18. Mean image offsets and their standard deviations in worm tracking at 8Hz, 15Hz, 20Hz and 30Hz, respectively.

7. Conclusion

This paper presents an entire tracking strategy for freely moving *Caenorhabditis elegans* by a 2-axis piezo stage. This strategy involves in two hierarchies—the basic one (single motion compensation step) and the upper one (motion tracking loop), which meets our requirements for both LBI and NCI. Our work extends previous efforts on real-time motion tracking of freely moving *C. elegans* with the following five contributions:

(1) Basing on the desired dark-field imaging, the worm ROI tracking could be in long-term and large motion travel over 60 mm.

(2) Under the 20Hz motion sampling, the mean motion step is less than 18 μ m and the mean motion response time is less than 80ms. In other words, the actual response rate of 2 axes is more than 12Hz. This ensures us to track the worm at relatively high speed of moving and still save enough time for NCI.

(3) Under the 20Hz motion sampling, the motion tracking errors in MTE₄ are less than 2.2 μ m and the single motion step accuracy is less than 1 μ m, which is much less than one pixel in LBI images.

(4) Under the 20Hz motion sampling, the mean offset in real-time tracking is less than 6 pixels and the standard deviation is 0.42 pixels. Smooth motion contributes to the high quality NCI images.

(5) A quantitative evaluation method for the tracking performances has been first given in this paper. It can quantitatively evaluate the tracking performances in different strategies as well as optimize the strategy in different parameters. Moreover, this tracking strategy can be suitable for most kinds of piezo stage based worm tracking systems, or even other kinds of motors in closed-loop.

In the future work, we are planning to implement a complicated synchronous tracking strategy to let two axes always start and stop motion at the same time, no matter the horizontal CMS and vertical CMS are neither similar nor different in number. That drives us to realize the speed control of piezo motor via PID parameters, rather than one axis waiting for another to stop mentioned in section 5.4. For this purpose, we need to build a two-dimension look-up table for both step value and response time in the basic hierarchy and then update the optimal frame rate of motion sampling in the upper hierarchy.

Funding

This work was supported by the Ministry of Science and Technology of China through the Basic Research Program (973) 2011CB809105, by the Natural Science Foundation of China grant 61101156, 91232715, 61421062, 61520106004, 61375022, by the Open Research Fund of the State Key Laboratory of Cognitive Neuroscience and Learning grant CNLZD1404, by the Beijing Municipal Science and Technology Commission on contract Z151100000915070.

Acknowledgement

We are very grateful to Dr. Yan Zhu for some valuable discussions, and our colleague Dr. Dong Liu, Dr. Pengpeng Liu, Yongjun Li and Mengxi Guo for *Caenorhabditis elegans* strain N2 and *Prab-3::nls-RSET-GCaMP6s:SL2::nls-TagRFP::unc-54utr* transgenic worm.